Title

Daylight-driven rechargeable antibacterial and antiviral nanofibrous membranes for bioprotective applications.

Journal

Science advances, 4(3)

ISSN

2375-2548

Authors

Si, Yang
Zhang, Zheng
Wu, Wanrong
et al.

Publication Date

2018-03-01

DOI

10.1126/sciadv.aar5931

Peer reviewed

MATERIALS SCIENCE

Daylight-driven rechargeable antibacterial and antiviral nanofibrous membranes for bioprotective applications

Yang Si,[1] Zheng Zhang,[1] Wanrong Wu,[1] Qiuxia Fu,[2] Kang Huang,[3] Nitin Nitin,[3] Bin Ding,[2] Gang Sun[1]*

Emerging infectious diseases (EIDs) are a significant burden on global economies and public health. Most present personal protective equipment used to prevent EID transmission and infections is typically devoid of antimicrobial activity. We report on green bioprotective nanofibrous membranes (RNMs) with rechargeable antibacterial and antiviral activities that can effectively produce biocidal reactive oxygen species (ROS) solely driven by the daylight. The premise of the design is that the photoactive RNMs can store the biocidal activity under light irradiation and readily release ROS under dim light or dark conditions, making the biocidal function "always online." The resulting RNMs exhibit integrated properties of fast ROS production, ease of activity storing, long-term durability, robust breathability, interception of fine particles (>99%), and high bactericidal (>99.9999%) and virucidal (>99.999%) efficacy, which enabled to serve as a scalable biocidal layer for protective equipment by providing contact killing against pathogens either in aerosol or in liquid forms. The successful synthesis of these fascinating materials may provide new insights into the development of protection materials in a sustainable, self-recharging, and structurally adaptive form.

INTRODUCTION

Public health outbreaks driven by emerging infectious diseases (EIDs) constitute the forefront of global safety concerns (*1*, *2*). EID outbreaks, such as severe acute respiratory syndrome, avian influenza, and Ebola virus disease (EVD), have shaped the course of human history and caused incalculable misery and death (*3*, *4*). This issue was highlighted by the 2014 EVD epidemic crisis in West Africa, a total of 28,646 confirmed cases with 11,323 deaths, which was an explicit example of unpreparedness of the public health system (*4*). In particular, the risk of acquisition of an EID during the care of a patient is significantly high for health care workers (HCWs) (*5*). Although the HCWs did their best to control the recent EVD outbreaks, 852 HCWs were diagnosed with Ebola, and 492 of them died (*6*, *7*). The infection incidence among HCWs became 100 times higher than that of the general population (*7*). To prevent the transmission of EID spread in a workplace, HCWs are advised to wear personal protective equipment (PPE), including face masks, bioprotective suits, and medical gloves, according to the standard infection prevention and control guidance (*8*, *9*). Although these PPE can significantly minimize the pathogen transmission, the risk of infection cannot be entirely eliminated (*9*). EID pathogens can be effectively captured and intercepted by the relevant protective materials; however, the sustained infection activity of the pathogen could easily cause cross-contamination and postinfection, which might lead to increased risk of pathogen spreading (*10*, *11*). Alternatively, antimicrobial active protective technologies by incorporating biocidal agents into PPE materials could be another strategy to provide promising bioprotection against EID pathogens because direct contact killing is achieved (*12*, *13*). Various biocides, such as triclosan, nisaplin, essential oils, peptide, chitosan, and silver nanoparticles, have recently been incorporated for bioprotective applications (*14*–*18*). However, their immediate biocidal effect usually suffers from significant decline due to the irreversible consumption of the biocides (*19*). More effective, easy-to-use, field-deployable, and durable PPE materials to provide antimicrobial bioprotection from infection source to point-of-use are needed, particularly for the outdoor emergency medical services.

A systematic design of desired antimicrobial bioprotective materials requires an optimization of two important characteristics: the biocidal activity, as a capacity of the killing of microbial pathogens, and the renewability of the biocidal functions, which affects the durability and reusability in a long-term usage (*20*, *21*). Rechargeable biocidal halamine materials have been developed and extensively investigated in recent years, and their functions can meet the basic requirements of bioprotection (*22*, *23*). However, the use of a chlorine bleach solution as a recharging agent puts limitations on applications. Photo-induced antimicrobial materials, as the forefront of advanced and green materials, have high biocidal efficiency, ease of activity recharging, broad-spectrum biocides, long-term stability, high durability, and low toxicity with little environmental concern (*24*, *25*). These materials would be, in this regard, a great promise as an exceptional candidate for constructing bioprotective equipment. Despite their outstanding potential, the major problem associated with the photoantimicrobial materials is their solely photo-driven biocidal character, with the instantaneous biocidal function fast decaying or quenching under dim light and dark conditions (*26*, *27*). Moreover, most of these products were driven by high-energy ultraviolet (UV) light rather than the readily available daylight source (*28*, *29*), which are often energetically and operationally intensive, focused on specialized UV irradiation systems, thus significantly limiting the usability for bioprotection. Therefore, the challenge is to construct a daylight-driven, rechargeable, and antimicrobial material capable of working under both light and dark conditions, without compromising the interception performance against tiny pathogenic particles.

Here, we present a robust methodology to create daylight-driven rechargeable antibacterial and antiviral nanofibrous membranes (RNMs) by incorporating daylight-active chemicals that can effectively and efficiently produce reactive oxygen species (ROS). The photoactive RNMs can store the biocidal activity under light irradiation and readily release ROS to provide biocidal functions under dim light or dark conditions. The RNMs exhibit integrated properties of fast ROS production, ease of activity storing, long-term durability, high biocidal efficacy, robust

[1]Fiber and Polymer Science, University of California, Davis, Davis, CA 95616, USA. [2]Key Laboratory of Textile Science and Technology, Ministry of Education, College of Textiles, Donghua University, Shanghai 201620, China. [3]Departments of Food Science and Technology and Biological and Agricultural Engineering, University of California, Davis, Davis, CA 95616, USA.
*Corresponding author. Email: gysun@ucdavis.edu

breathability, and interception of fine particles. The incorporation of RNMs as a biocidal surface protective layer on protective equipment was demonstrated to achieve promising contact killing against pathogens either in aerosol or in liquid forms.

RESULTS

Synthesis and biocidal functions of RNMs

We prepared the RNMs based on three criteria: (i) The membranes can effectively intercept pathogen particles via porous nanostructure, (ii) the membranes must become biocidal under daylight irradiation, and (iii) the membranes must be able to store the biocidal activity and readily release it under dark conditions. The first requirement was satisfied by using micro/nanotextured membranes with small pore sizes; ultrafine electrospun nanofibers were used as templates to achieve a breathable interception barrier. To satisfy the other two criteria (the formation of rechargeable biocidal functions), our molecular design is based on benzophenones and polyphenols, which are widely used as photosensitizers in biochemistry and organic synthesis (*30*). The biocidal activity came from the generated ROS when they were exposed to light irradiation in the presence of oxygen (*30*, *31*). Figure 1A describes the synthesized structures. Two classes of benzophenone with different substitutes, 4-benzoylbenzoic acid (BA) and benzophenone tetracarboxylic dianhydride (BD), and a natural polyphenol, chlorogenic acid (CA), were selected as the photobiocides to bring about the biocidal functions. Poly(vinyl alcohol-*co*-ethylene) (PVA-*co*-PE) was used as a polymer precursor and hydrogen donor to construct the nanofibrous networks (*32*). The fabrication began with a production

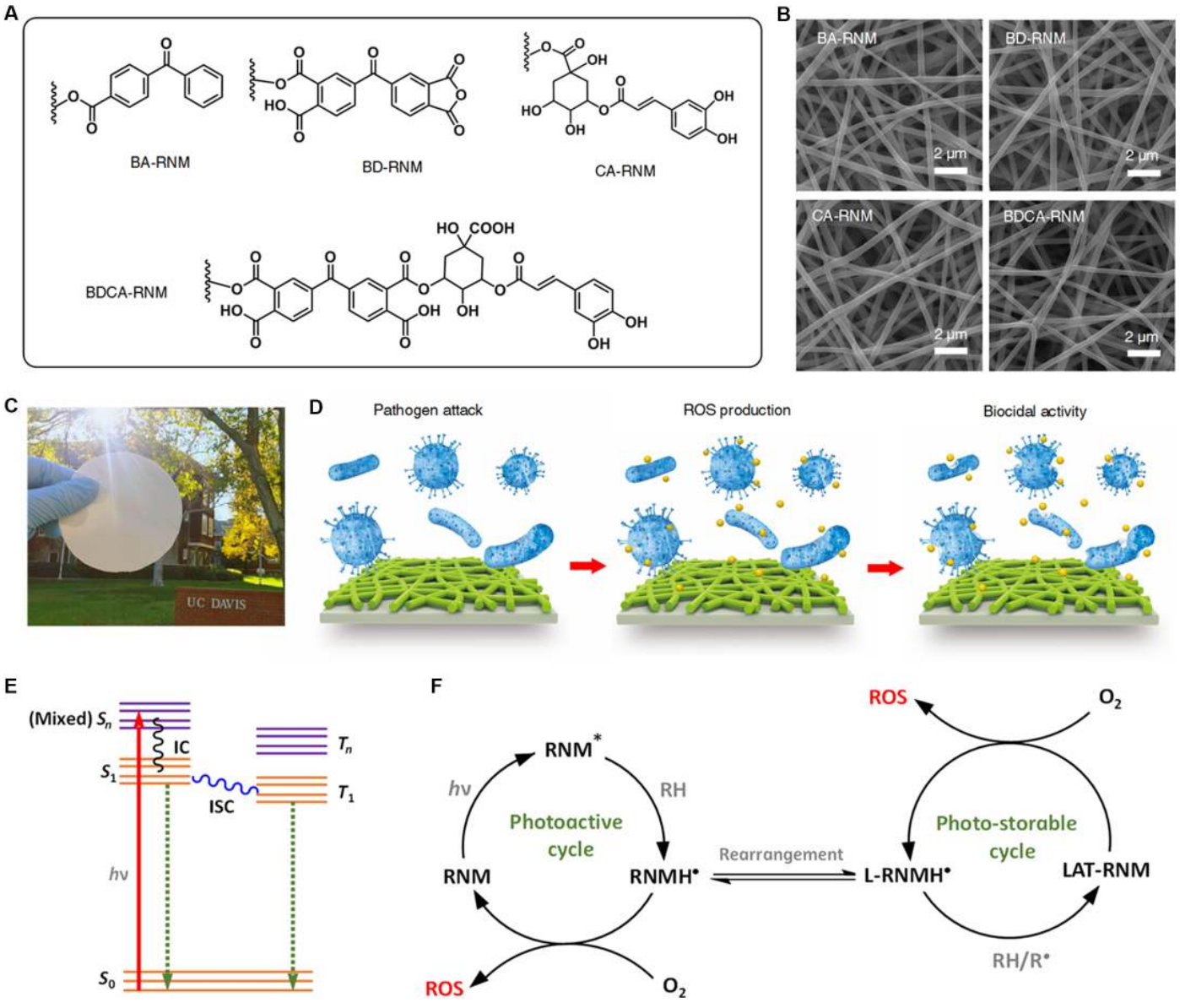

Fig. 1. Design, structure, and biocidal function of RNMs. (**A**) Chemical structure of BA-RNM, BD-RNM, CA-RNM, and BDCA-RNM. (**B**) Microscopic architecture of various RNM samples. (**C**) Optical photograph of the BDCA-RNM sample. (**D**) Schematic demonstration of the biocidal functions of RNMs by releasing ROS. (**E**) Jablonski diagrams representing the singlet excitation and following ISC to triplet. (**F**) Proposed mechanism for the photoactive and photo-storable biocidal cycles.

of PVA-*co*-PE nanofibrous membranes in an average fiber diameter of 226 nm by electrospinning (fig. S1). Subsequently, grafting reactions were conducted by immersing the membranes in tetrahydrofuran solution with various photosensitizers, and the esterification reactions between the hydroxyl groups on the membrane with carboxyl groups of the agents were catalyzed by carbonyldiimidazole (CDI) (see details in figs. S2 to S5). Thereafter, the resulting membranes were washed with acetone and dried in vacuum to remove any residual solvents. The nanofibrous membranes modified by BA, BD, and CA were abbreviated as BA-RNM, BD-RNM, and CA-RNM, respectively. In anticipation that the combination of benzophenone and polyphenol moieties might bring in a synergistic effect in photoactivity, the BD-RNM was further grafted with CA to obtain BDCA-RNM samples (fig. S6). The representative field-emission scanning electron microscopy (FE-SEM) image of the relevant samples presented in Fig. 1B revealed randomly oriented three-dimensional nonwoven morphology with fiber diameters in the range of 200 to 250 nm. Obvious adhesive was observed among nanofibers, which could be attributed to the superficial swell of nanofibers during the grafting reactions. Because of the simplicity of the modification process and the facile availability of electrospun nanofibers, great versatility in controlling the thickness and scaling up the synthesis is feasible. Figure 1C shows a typical BDCA-RNM with a thickness of 20 μm, and other samples with the thickness from 5 to 100 μm were readily prepared (fig. S7). A large-scale BDCA-RNM sample with a size of 40 × 40 cm^2 can also be prepared using a multi-needle spinning device (fig. S8).

Figure 1D demonstrates the biocidal effect of the RNMs against pathogenic microbes. Once the pathogens are intercepted and in contact with the surface of the nanofibers, the grafted photobiocides could display an intrinsic biocidal activity as free chemicals; that is, in the presence of oxygen, various ROS, including hydroxyl radicals (•OH), superoxide ($•O^{2-}$), and hydrogen peroxide (H_2O_2), are produced continuously under light irradiation. ROS could further rapidly damage DNA, RNA, proteins, and lipids, resulting in bacterial death and virus inactivation (*33*, *34*). Our proposed mechanism of the photoactive and photo-storable biocidal functions is demonstrated in Fig. 1 (E and F). The initial photoreaction hinges on the ability of the photoexcited RNM to access the triplet excited state (^{3}RNM*) via intersystem crossing (ISC), which may be of local excitation or charge transfer character, depending on the relative configuration of the π* orbital. Thereafter, ^{3}RNM* can abstract a hydrogen atom from a hydrogen donor to form a quinone radical (RNMH•). Under aerobic conditions, the RNMH• would be trapped by oxygen molecules, going back to RNM and simultaneously yielding active ROS (*35*, *36*). Meanwhile, if the generated RNMH• was not fully quenched by oxygen, then a competing reaction, including structure rearrangement and a second hydrogen abstraction, could occur, leading to the formation of a metastable structure that stores the activity. This activity could readily release in the form of generating ROS, even under dark conditions. The detailed reactions related to the photoactive and photo-storage cycles are schematically presented in fig. S9.

Photoactivity of RNMs

To provide insight into the excitation features of the RNMs, we used time-dependent density functional theory (TD-DFT) calculations and diffuse reflection UV-visible (UV-vis) spectroscopy to evaluate the nature of the initial photoexcitation event. The TD-DFT calculations of the RNMs (see details in table S1) predict that the lower energy S_0 (ground state) → S_1 (lowest singlet excited state) excitations are negligible with very weak oscillator strength. Meanwhile, the $S_0 \rightarrow S_n$ excitations of the RNMs are predicted to be dominant, and the calculated maximum wavelength (λ_{max}) matched with the measured UV-vis spectra, as shown in Fig. 2 (A to D). The λ_{max} of BA-RNM, BD-RNM, CA-RNM, and BDCA-RNM were 275, 307, 336, and 332 nm, respectively. Although these λ_{max} values were mainly located in the UV range, compared with the standard spectrum of D65 daylight, the light energy in the range from 300 to 450 nm can still be readily used by the RNMs, as shown in Fig. 2E. The estimated daylight absorbance coefficients ($\int_{300}^{450} I_\lambda d\lambda / \int I_\lambda d\lambda$) for BA-RNM, BD-RNM, CA-RNM, and BDCA-RNM were 21.62, 35.33, 66.04, and 45.41%, respectively, indicating a robust utilization of daylight source. After initial photon absorption, fast relaxation via internal conversion results in thermalization of the excited electron from S_n to the S_1, followed by ISC to the T_1 (lowest triplet excited state), where a series of photoreactions could originate (*36*, *37*). Inspection of the frontier orbitals of T_1 reveals qualitative differences in these RNMs. The BA-RNM and BD-RNM have similar n_{HOMO}-π_{LUMO} transitions in T_1, with both *n* electron localized on carbonyl group and π electron localized over the entire conjugate system. In contrast, the CA-RNM exhibited a typical π_{HOMO}-π_{LUMO} transition with both π and π* orbitals localized on a phenyl ring system. Moreover, by the combination of the benzophenone and the polyphenol, the T_1 of BDCA-RNMs exhibits a unique charge transfer character with a n_{HOMO}-π_{LUMO+3} transition (*38*), where an electron occupying the HOMO orbital, which is an *n* orbital localized on the carbonyl group in benzophenone, is promoted into the spatially separated π*LUMO+3 localized on the conjugated system of CA.

To test the photoactivity of relevant RNMs, we equipped a daylight irradiation device with an irradiance of 6.5 mW cm^{-2} and a facile availability of light source [D65 standard daylight tube (GE F15T8/D)] and measured the formed ROS in terms of two typical species: OH• and H_2O_2 (*36*). The relevant RNMs were subjected to a cyclic irradiation test with 20-min interval light-dark fatigue cycles. As shown in Fig. 2 (F and G), generation of OH• and H_2O_2 was mainly observed during irradiation and paused during dark periods, and the amount of ROS steadily increased after irradiation with no significant decrease in activity. The BD-RNM and BDCA-RNM exhibited robust photoactivity, whereas the BA-RNM and CA-RNM only showed poor ROS generation capacity. Significantly, the BDCA-RNMs exhibited the highest OH• and H_2O_2 generation capacities of 49.96 and 15.26 μg g^{-1} min^{-1}, respectively, which were one to two orders of magnitude higher than those of other daylight-driven photoactive materials (*26*, *39*).

The photo-induced ROS generation cycle involves the hydrogen abstraction (RNMH•/^{3}RNM) by the triplet RNMs and a subsequent oxidation (RNM/RNMH•) by oxygen. To provide insight into the mechanism of the photo-induced reaction, we used DFT to calculate the energy of the relevant reaction moieties (see details in table S2). We also quantified the reaction feasibility using Gibbs free energy change (Δ*G*). As shown in Fig. 2H, both BA-RNM and BD-RNM exhibited obvious negative Δ*G* (RNM/RNMH•) and Δ*G* (RNMH•/^{3}RNM), revealing that the hydrogen abstraction and oxidation reactions were highly spontaneous. However, the poor daylight absorption ability of BA-RNM resulted in its weak photoactivity. In contrast, the CA-RNM showed significantly high Δ*G* (RNM/RNMH•) of 290 kJ mol^{-1} due to the inactive π-π triplet transition, which means that the hydrogen abstraction largely does not occur to form active radicals; thus, further ROS generation was also disabled despite the high excitation rate. Moreover, benefiting from the unique charge transfer feature of *n*-π transition, the BDCA-RNM exhibited high reactivity for both inter- and intramolecular photoreaction (see details in fig. S10), leading to the

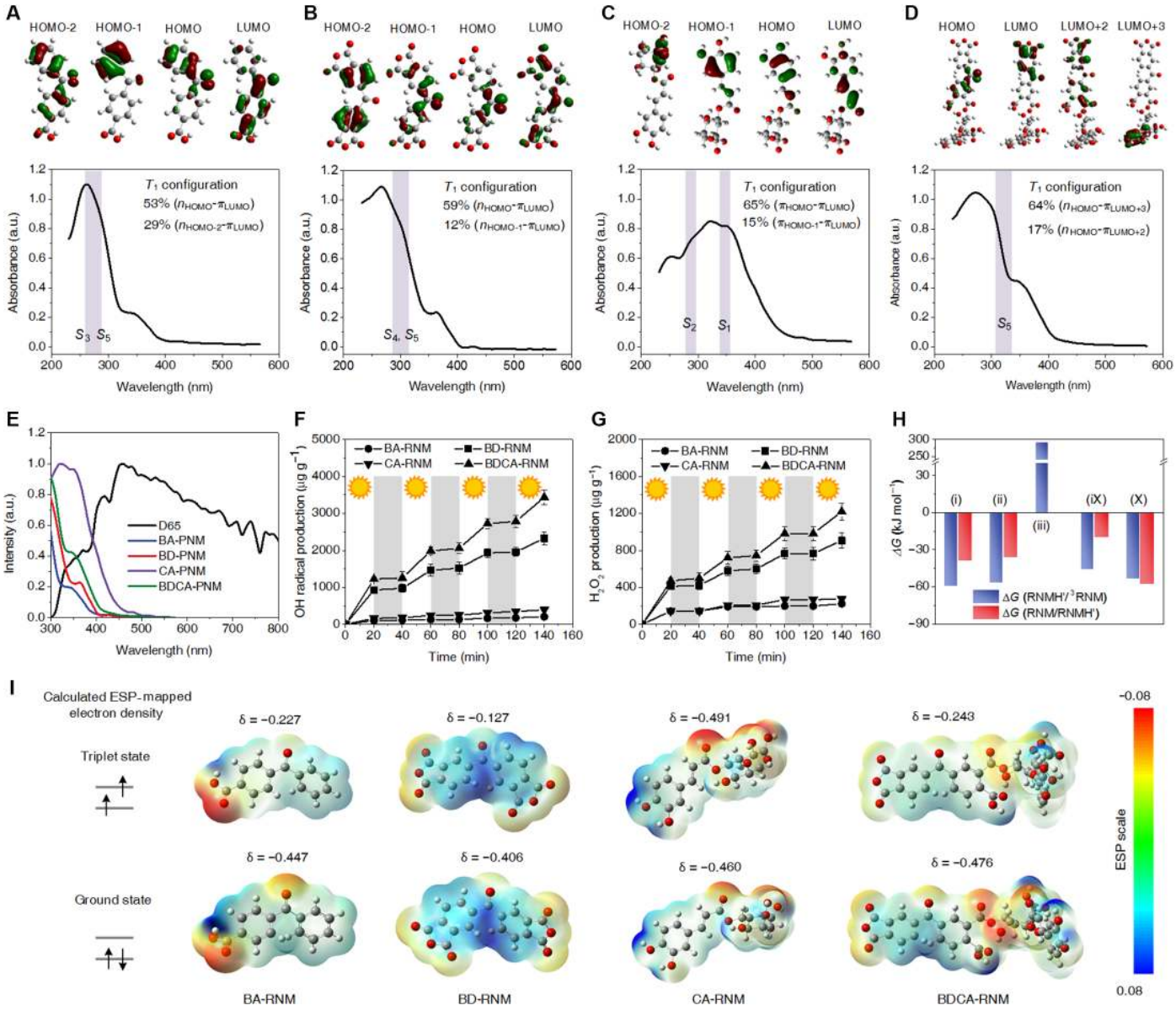

Fig. 2. Photoactivity and excitation features of the RNMs. (**A** to **D**) Diffuse reflection UV-vis spectra of BA-RNM (A), BD-RNM (B), CA-RNM (C), and BDCA-RNM (D) along with theoretically assigned percentage contributions (>10%) of T_1 orbitals; the acronyms of HOMO and LUMO stand for highest occupied molecular orbital and lowest unoccupied molecular orbital, respectively. λ_{max} is the predicted maximum absorption wavelength. a.u., arbitrary units. (**E**) Normalized UV-vis spectra of various RNMs samples along with the spectrum of the D65 standard light source. (**F** and **G**) Quantification of OH• (F) and H_2O_2 (G) generated by various RNMs samples versus time (irradiation in white and dark periods in gray). (**H**) Calculated ΔG of RNMH•/^{3}RNM* and RNM/RNMH• transition. The i, ii, iii, iX, and X represent BA-RNM, BD-RNM, CA-RNM, inter–BDCA-RNM, and intra–BDCA-RNM, respectively. (**I**) ESP-mapped electron density of the ground state and T_1 state of various RNMs samples. The values of δ were the ESP charge on oxygen atoms in the carbonyl group.

robust ROS generation efficiency (*38*, *40*). These results were further supported by the electrostatic potential (ESP)–mapped electron density of the T_1 and ground state of these RNMs. As shown in Fig. 2I, the T_1 states of BA-RNM, BD-RNM, and BDCA-RNM exhibited obvious electron deficiency character on the oxygen atom in the carbonyl group compared with the ground state, implying the high tendency for hydrogen abstraction (*35*, *41*). In contrast, a slight increase of ESP in carbonyl oxygen was observed for CA-RNM, resulting in the inactive T_1 states. From these results, we propose that the photoactivity of the RNMs is dictated both by the light-absorbing capability (that is, the transition to singlet state) and by the character of the T_1 triplet state (excitation configuration and structure of frontier orbital).

Rechargeable capability of RNMs

The properties of photoactive nanofibrous-structured RNMs can be further demonstrated by their promising rechargeable biocidal functions. We have indicated that the photoactive cycle consists of the excitation, hydrogen abstraction, and quenching by oxygen. However, if the generated RNMH• was not fully quenched by oxygen or other organic burdens (for example, microbes), then other competing reactions

related to activity storage could occur. To demonstrate this, we irradiated the relevant RNMs under daylight with increasing exposure time to 60 min and studied the photo-induced reaction and structure rearrangement with UV-vis spectroscopy and TD-DFT calculations, as shown in Fig. 3 (A to D). The BA-RNM shows an obvious absorption peak shift from 262 to 252 nm, characteristic of the formation of reduced moieties in diphenylmethanol (DPM) form (fig. S11) (*41*). Meanwhile, besides the DPM formation, a distinct absorption increase was observed at 420 nm for BD-RNM, indicating the formation of a metastable transient photoproduct that was previously referred as the light-absorbing transient (LAT) moieties (fig. S12) (*42*, *43*). Similarly, the BDCA-RNM exhibited an even more distinct LAT formation without DPM transition. No visible change was recorded for CA-RNMs, which was due to the poor hydrogen abstraction ability. The formed DPM photoproduct was quite stable and was not able to go back to the original benzophenone statues (fig. S13). Meanwhile, the LAT moieties were proven to be oxygen-sensitive and can be readily quenched and reversed to benzophenone by reducing agents in the presence of oxygen (fig. S14), regenerating the photoactivity (*42*, *44*). A detailed mechanistic proposal for the rechargeable reactions of RNMs in the presence of oxygen is shown in Fig. 3E.

We further compared the photo-induced structural reorganization of RNMs by typical absorption intensity change related to DPM (262 nm) and LAT (420 nm) structures. As shown in Fig. 3F, the BDCA-RNM exhibited negligible DPM formation while having the maximum LAT transition ability, indicating that the activity-stored structure was able to recover with rare functional decaying. To quantify the ROS rechargeable capability, we first charged the relevant RNMs by 1 hour of daylight irradiation and then measured the releasing activity under dark conditions in terms of the amount of OH• and H_2O_2. As shown in Fig. 3 (G and H), in contrast to the gradual ROS generation in irradiation tests, the RNMs rapidly released more than 90% of ROS in the first 5 min, and after that, the releasing ability shows a saturation region with ROS amount increasing slowly. As expected, the BDCA-RNM exhibited the highest recharging capacity, with OH• and H_2O_2 releasing amounts of 2332 and 670 μg g^{-1} by 1 hour of daylight charging, corresponding to the charging rates of 38.86 and 11.16 μg g^{-1} min^{-1}, respectively, which means that the light energy was largely used with more than 70% conversion efficiency compared to the irradiation tests. Moreover, the recharging cyclic test of BDCA-RNM was performed as displayed in Fig. 3I. For each cycle, the BDCA-RNM samples were first irradiated for 1 hour and were fully quenched with an excess amount of

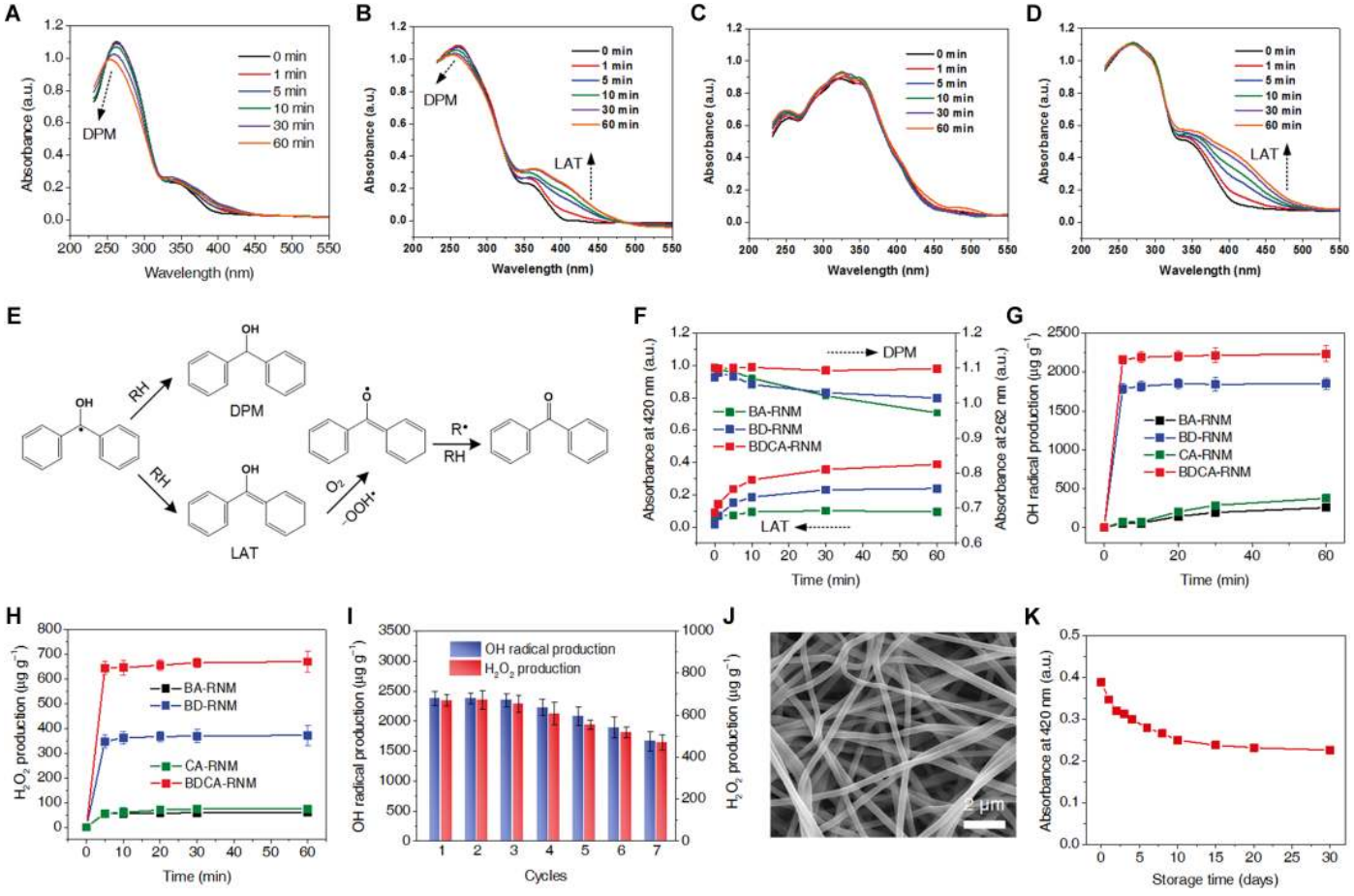

Fig. 3. Photo-induced rechargeable biocidal functions of RNMs. (**A** to **D**) UV-vis spectra of BA-RNM (A), BD-RNM (B), CA-RNM (C), and BDCA-RNM (D) under increasing daylight irradiation time. (**E**) Schematic description of the formation of the DPM and LAT structures. (**F**) Representative absorbance at 262 (DPM) and 420 nm (LAT) as a function of irradiation time. (**G** and **H**) Quantification of OH• (G) and H_2O_2 (H) released by various RNMs under dark conditions after 1 hour of daylight irradiation. (**I**) Rechargeable capability of BDCA-RNM when repeatedly charging and quenching over seven cycles. (**J**) FE-SEM images of BDCA-RNM after seven cyclic recharging tests. (**K**) Change of LAT structure of BDCA-RNM versus storage time.

a thiosulfate solution. No significant decrease in the recharging capacity was observed for BDCA-RNM after seven cyclic tests; they retained more than 75% of the original charging amount of OH• and H_2O_2. The nanofibrous architecture was also well maintained during the seven cycles of recharging, as demonstrated in Fig. 3J. The slight decrease of the capacity could be attributed to the accumulative consumption of the nonrenewable tertiary hydrogen in the PVE-*co*-PE nanofiber matrix (*35*, *42*). In addition, stability for long-time storage of the LAT structure is another practical concern for recharging performance. The decay of the LAT structure occurred notably on the existence of oxygen and reductive organic matter, which could lead to a quick release of ROS. Therefore, if the RNMs were stored under a dry and closed condition, then the absorption peak associated with the LAT structure should exhibit slow decays, which can be observed in Fig. 3K. A storage test over 30-day measurements revealed that the BDCA-RNM still retained more than 55% of the original LAT structure, highlighting the structural stability.

Contact killing against bacteria and virus

To evaluate the antibacterial activity of the RNMs, we challenged the membrane surface with two typical pathogenic bacteria, Gram-negative *Escherichia coli* O157:H7 and Gram-positive *Listeria innocua*. For the contact-killing assay, the control (pristine PVA-*co*-PE nanofibrous membranes) and BDCA-RNM samples with a size of 2×2 cm^2 were loaded with 10 μl of 1×10^8 colony-forming units (CFU) of a bacterial suspension (2.5×10^5 CFU cm^{-2}), and the bacterial proliferation was assessed by agar plate counting. Figure 4A depicts the time-dependent antibacterial effect of the BDCA-RNM under daylight irradiation conditions. It was found that the control samples showed significant bacterial growth during incubation even after 1 hour of irradiation. In contrast, the BDCA-RNM showed effective killing of bacteria, achieving 6 log CFU reduction of *E. coli* and *L. innocua* in 60- and 30-min daylight irradiation, respectively, which corresponds to a promising contact-killing efficacy of 99.9999%. In comparison, a contact time of 5 to 10 hours is typical for previous photoactive hydrogels to achieve these bacterial reductions (*45*, *46*), and other photoactive fibrous materials exhibit only up to 4 log CFU reduction but require a contact time of several hours (*28*, *47*). Moreover, in marked contrast to the traditional photoantimicrobial materials, the BDCA-RNM can store the biocidal activity and kill bacteria under dark conditions, as shown in Fig. 4B. After 1 hour of daylight exposure, the charged BDCA-RNM exhibited 6 log CFU reduction of both *E. coli* and *L. innocua* within 120-min contact under dark conditions, which nearly maintained half of the biocidal efficiency compared with the conditions of under lighting. Considering that the HCWs are easy to experience dim light or dark working conditions, this rechargeable biocidal performance is very promising on PPE from the viewpoint of practical bioprotection, serving the biocidal function "always online." In addition, the rechargeable feature is also responsible for the renewed cyclic performance of the RNMs against microorganisms. As shown in Fig. 4 (C and D), the five cyclic contact-killing tests revealed that the biocidal efficacy was nearly constant with 6 log CFU reduction of the bacteria, no matter with or without light exposure, highlighting the biocidal character of the BDCA-RNMs.

To gain insight into the bactericidal mechanism of the RNMs, we investigated the morphological changes of bacteria after contacts with the RNMs. As shown in Fig. 4 (E to H), both *E. coli* and *L. innocua* cells contacting with the control samples remained smooth and in their respective rodlike morphologies with intact cell membranes. In sharp contrast, cellular deformation and surface collapse were found on the bacterial cells after exposure to the BDCA-RNM after 1 hour of light exposure. Most of the cells were lysed, and numerous small portions of debris were observed. This observation was also supported by the live/dead bacterial fluorescence staining assays. The bacteria in contact with the control and BDCA-RNM were washed out and first stained with a cell-nonpermeant propidium iodide (PI) red dye, which is only able to penetrate cells with compromised membranes, and then, they were counterstained with a cell-permeant SYBR Green (SG) dye, which can stain the nucleic acids of both intact and permeabilized cells. As shown in Fig. 4 (I to L), numerous live *E. coli* and *L. innocua* were observed in green color after contacting the control samples, whereas little red color was found. In contrast, upon 1-hour contact with the BDCA-RNM under light conditions, the observed green fluorescence signals were significantly decreased, and all cells in green color were almost exclusively in red color as well, revealing that most of bacterial cells were disrupted or lysed without any integrated morphology. To further assess the damage induced on bacterial cell membranes, we detected leakage of nucleic acids and proteins from the bacterial cells after contacting with BDCA-RNM samples. Supernatants of pelleted culture were analyzed for spectrophotometric absorbance readings at 260 and 280 nm, which corresponded to the characteristic peaks of nucleic acids and proteins, respectively. As shown in Fig. 4 (M and N), nearly no organic matter was detected from the supernatant after contacting with the control samples. Meanwhile, significant leakage of nucleic acids and proteins was observed for the *E. coli* and *L. innocua* after contacting with BDCA-RNM, either under light exposure or under dark conditions, confirming the disruption of the bacterial cell walls and membranes. These results suggested that the bactericidal function of the BDCA-RNMs should be similar to that of peroxide disinfectants commonly used in medical sterilization, which involve bacterial cell wall and membrane disruption (*33*, *48*). Moreover, contact killing and free ROS release are both possible mechanisms, but the contact killing plays a dominant role for the RNMs. Because the ROS radicals have a quite short lifetime of <10 μs with negligible migration distance, the stable H_2O_2 was not able to reach the critical biological activity level in such a short time (<10 min) (*30*, *33*). Therefore, the use of the RNMs is advantageous to avoid the undesirable free ROS release and accumulation by using ROS smartly, effectively, and safely.

Antiviral function, killing or inactivating viruses, is another essential requirement for bioprotective PPE materials, especially for the increasingly viral outbreaks that the public is facing today. To evaluate the antiviral performance of the RNMs, we tested the membrane surface with T7 bacteriophage and evaluated the viral activity by *E. coli*–based stationary phase plating assay. T7 phage is a nonenveloped double-stranded DNA virus and has a single proteinaceous capsid, which has been shown to be less sensitive to photodynamic destruction than enveloped or RNA-based viruses (*48*). Therefore, T7 phage is an appropriate viral model to test the reduction of viruses by contact with the RNMs. As shown in Fig. 4 (O and P), nearly no contact killing was observed on the control samples, and the harvested phages could grow and proliferate freely on the *E. coli*–based culture medium. In contrast, the BDCA-RNM showed rapid and effective killing of T7 phage, achieving 5 log of PFU (plaque-forming units) reduction even in 5-min contact under daylight exposure. The charged BDCA-RNM also achieved 5 log of PFU reduction within 30 min of contact under dark conditions. The fast and highly effective biocidal activities were significantly superior to the previously reported photo-induced antiviral materials (*26*, *49*). Moreover, compared with

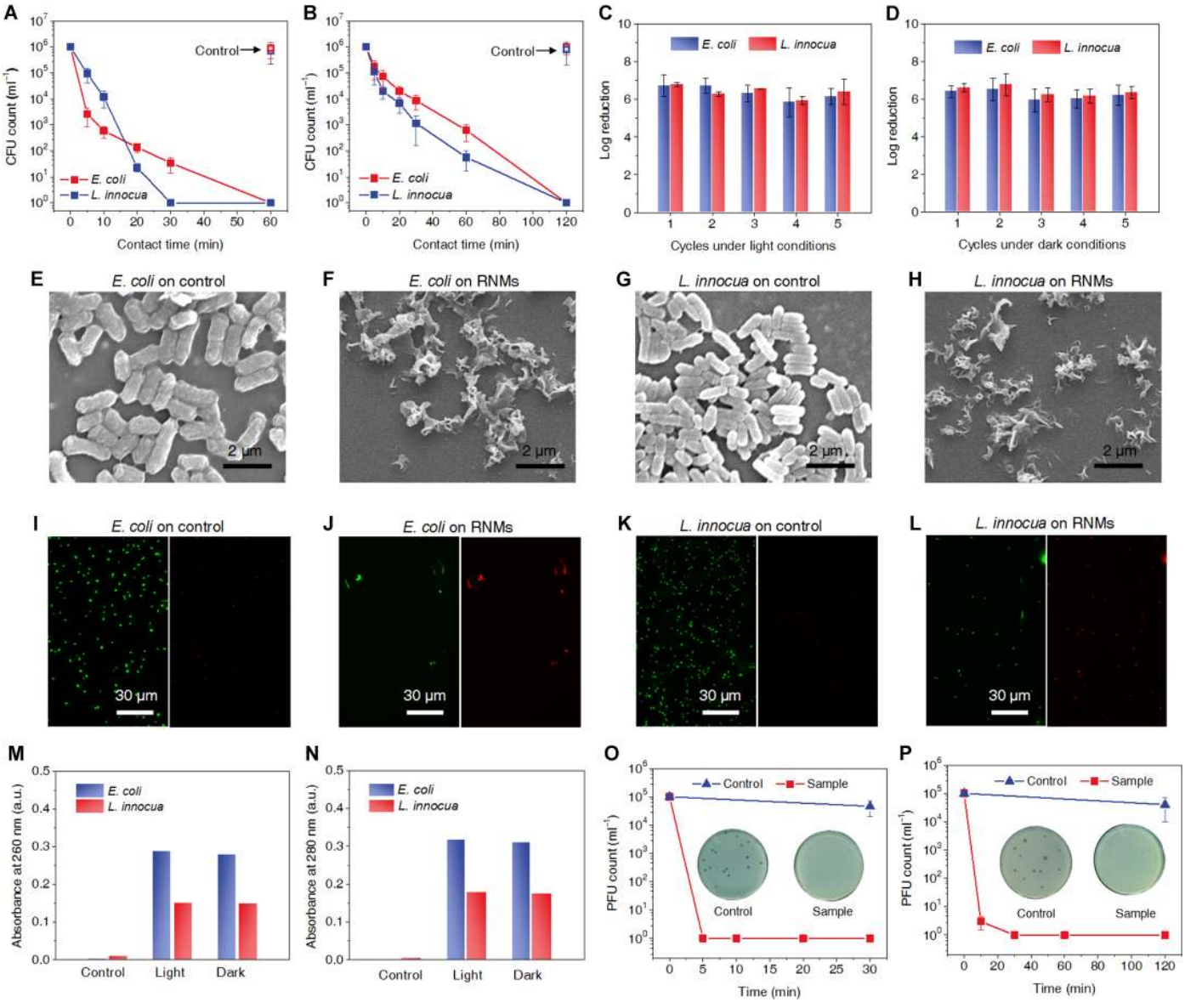

Fig. 4. Antibacterial and antiviral properties of BDCA-RNM. (**A** and **B**) Bactericidal activity against *E. coli* and *L. innocua* of BDCA-RNM under daylight irradiation (A) and charged BDCA-RNM under dark conditions (B). (**C** and **D**) Five cycle antibacterial test of BDCA-RNMs under daylight irradiation (C) and charged BDCA-RNMs under dark conditions (D). (**E** to **L**) Morphology (E to H) and live/dead bacterial viability assay (I to L) of *E. coli* and *L. innocua* cells in contact with control membranes and BDCA-RNM with 1-hour daylight irradiation. (**M** and **N**) Measurement of the leakage of nucleic acid (M) and proteins (N) from *E. coli* and *L. innocua* cells. (**O** and **P**) Biocidal assay against T7 phage for BDCA-RNM under daylight irradiation (O) and charged BDCA-RNM under dark conditions (P).

the above bacterial-killing results, the virus has shown more susceptibility to the photoactive RNM samples. This is because the ROS might easily cause cross-linking of capsid proteins in viruses, resulting in a direct impairment of the capability to bind to the host surface (*48*, *50*).

Bioprotection application of RNMs

With the above results in mind, we further demonstrated the utilization of BDCA-RNM as a biocidal surface function layer for bioprotection applications. To facilely integrate it to current PPE materials, we investigated the interception properties of the BDCA-RNM against ultrafine particles. We carried out the filtration performance evaluation by using the polydisperse sodium chloride (NaCl) particles with a diameter of 300 to 500 nm under increasing airflow. As shown in Fig. 5A, by increasing the airflow from 10 to 90 liter min^{-1}, the filtration efficiency of the BDCA-RNMs exhibited a very slight decrease from 99.98 to 99.07%, which was distinctly higher than that of the N95 facial mask (95%), widely used by HCWs. Meanwhile, the pressure drops showed an increased trend directly proportional to the airflow, indicating a cellular-dominated permeation behavior similar to that of the open-cell porous structure (*51*). Significantly, the maximum pressure drop of the BDCA-RNM was 128 Pa at 90 liter min^{-1}, which was only a third of the pressure drop standard of the N95 facemask (350 Pa at 85 liter min^{-1}) (*8*), highlighting the robust breathability of the nanofibrous structure. The promising filtration efficiency was also confirmed by SEM observations;

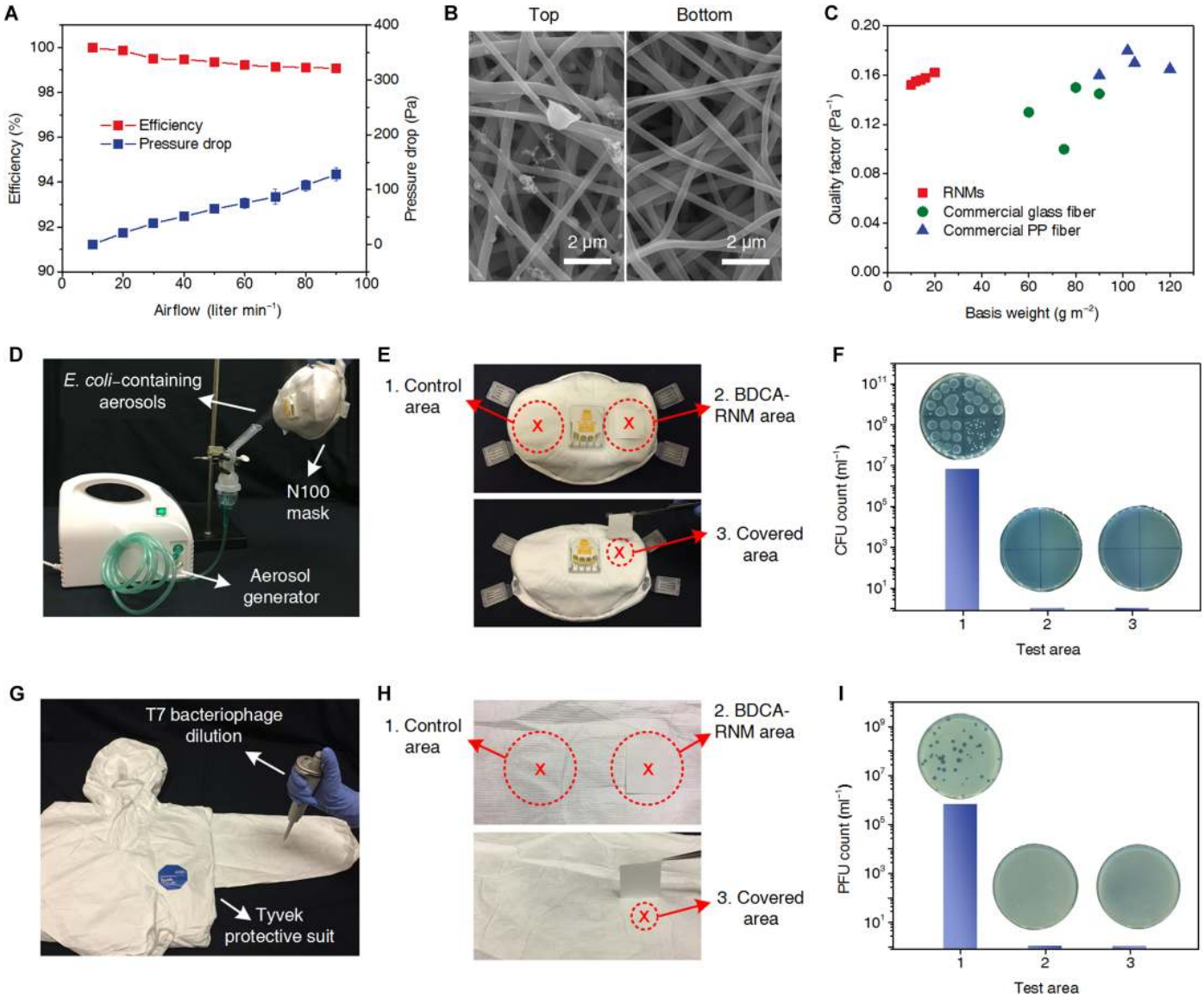

Fig. 5. Bioprotection performance of BDCA-RNMs. (**A**) Filtration efficiency and pressure drop of BDCA-RNM as a function of airflow. (**B**) SEM images of the top and bottom surface of BDCA-RNM after filtration (airflow of 90 liter min^{-1}, testing for 5 min). (**C**) QF values of selected fibrous filter materials with various basis weights. (**D**) Bacterial aerosol generation apparatus and the interception test by N100 mask. (**E** and **F**) Three selected test areas on the mask (E) and the relevant CFU count of *E. coli* (F). (**G**) Photograph showing the protective suit was loaded with T7 phage. (**H** and **I**) Three selected test areas on the protective suit (H) and the relevant PFU count of T7 phages (I).

from Fig. 5B, we can see that abundant particles were captured on the top surface of the BDCA-RNM, whereas no particles were observed on the bottom surface, and the membranes also well maintain their structural integrity during the filtration process with high airflow. To further visually evaluate the filtration capacity, we estimated the filtration quality factor (QF) of BDCA-RNM with different basis weight (Fig. 5C). The BDCA-RNM with $^1/_{10}$ of the basis weight exhibited the comparable QF values with current commercialized filtration materials, indicating the promising potential for protective applications (*51*, *52*).

As a proof of concept for bioprotective PPE application, the charged BDCA-RNM (1 hour of daylight irradiation) was stuck to the typical respirator and protective suit as a covering layer to bring the desired biocidal functions. It is well known that the transmission of pathogens contained in aerosol droplets plays a significant contribution to the spread of airborne diseases, and the surgical masks were suggested as the major inhalational barrier to protect HCWs (*8*, *10*). As shown in Fig. 5D, 1×10^6 CFU of *E. coli*–containing aerosols with the diameter of 1 to 5 μm were prepared as model infection aerosols, which was similar to the size of aerosols generated by a human sneezing or coughing. A charged BDCA-RNM with a size of 2×2 cm^2 was stuck on the right side of a 3M N100 respirator, and the respirator was exposed to a 0.2 ml min^{-1} of aerosols flow for 30 s. After standing for 30 min, the population of the living bacteria on the three representative areas—control area, BDCA-RNM area, and the covered area—were harvested and measured (Fig. 5E). As shown in Fig. 5F, the *E. coli* loaded on the control area exhibited high activity with free growth and proliferation, which was due to the nonbiological function of the traditional nonwoven materials. In contrast, no live bacteria were detected on the BDCA-RNM area or the

relevant covered area, indicating the robust protection against the pathogens. Similarly, the charged BDCA can also bring about promising bioprotection against the model virus to the typical protective suit, as demonstrated in Fig. 5 (G to I). These results indicate that the BDCA-RNM could serve as a scalable biocidal layer that not only intercepts but also effectively kills pathogens either in aerosols or in liquid forms, implying its potential broad applications in bioprotective PPE against the increasing EID threats.

DISCUSSION

The successful synthesis of RNMs provides the possibility of development of green bioprotective materials in a self-recharging, structurally adaptive, and nanofiber form. Here, PVA-*co*-PE–based RNMs served as a model system for the proof of concept. Considering the ease of scalable synthesis of electrospun nanofibers from various materials, this discovery will thus pave the way for new types of nanofiber-based RNMs made of polyurethane, polyamide, polyester, and polysulfone, which might open more windows for use in various protective applications. Biocompatible nanofibrous membranes [such as poly(lactic acid) and polycaprolactone] could also be used for RNMs fabrication, which might satisfy a stricter requirement for wound dressing. Moreover, the basic mechanism of the photoactive and photo-storable functions of RNMs was demonstrated; thus, we can expect that, similar to the selected benzophenones and polyphenols, a variety of other photosensitizers could be involved in RNMs synthesis, especially those natural, sustainable, and biocompatible chemicals such as plant phenols, flavonoid, alkaloid, carotenoid, and riboflavins. We thus can use computational modeling to discover even more efficient photosensitizers to design novel and green RNMs based on our proposed rules. Furthermore, by future combining biocompatible nanofiber matrix and photobiocides, the RNMs would open broad technological implications for tissue engineering, photodynamic therapy, bioactuators, medical therapy equipment, and smart wearable devices.

In conclusion, we have demonstrated a synergistic assembly strategy for the scalable fabrication of daylight-driven rechargeable antibacterial and antiviral materials through the combination of electrospun nanofibers and the daylight-active photosensitizers. The photoactive RNMs can store the biocidal activity under light irradiation and readily release ROS, providing biocidal functions under dim light or dark conditions. With their fast ROS production, ease of activity storing, long-term durability, and high biocidal efficacy, the RNMs can rapidly and effectively kill bacteria and viruses, either under light exposure or under dark conditions. We also demonstrated the incorporation of RNMs as a biocidal surface protective layer on protective equipment to achieve robust bioprotection against pathogens either in aerosol or in liquid forms.

MATERIALS AND METHODS

Materials

PVA-*co*-PE (ethylene content of 27 mol %), BA, 3,3′,4,4′-benzophenone tetracarboxylic dianhydride (BPTCD), CDI, tetrahydrofuran (THF), dioxane, acetone, chloroform, isopropanol, CDI, polyphosphoric acid (PPA), 25 weight % (wt %) glutaraldehyde solution, 37% formaldehyde solution, 4 wt % osmium tetroxide (OsO_4), potassium iodide, sodium hydroxide, ammonium molybdate tetrahydrate, potassium hydrogen phthalate, PI, and SG dye were purchased from Sigma-Aldrich. *p*-Nitrosodimethylaniline (*p*-NDA), CA, Luria-Bertani (LB) broth, LB agar, Tryptic soy broth, and Tryptic soy agar (TSA) were purchased from Thermo Fisher Scientific. Phosphate-buffered saline (PBS) and tris-buffered saline were obtained from USB Co. Ltd.

Preparation of PVA-*co*-PE nanofibrous membranes

The electrospinning solution was prepared by dissolving PVA-*co*-PE (M_n = 90,000; Sigma-Aldrich) in a mixture of water and isopropanol (weight ratio of 3:7) at 85°C with stirring for 4 hours; the concentrations of PVA-*co*-PE was 7 wt %. Afterward, the solution was transferred to a 20-ml syringe capped with a 6-gauge needle. A programmable syringe pump (Kent Scientific) was used to feed the solution with a constant rate of 2 ml $hour^{-1}$. A high voltage of 28 kV (EQ30, Matsusada Inc.) was applied to the needle, resulting in a generation of a continuous charged polymer jet. The resulting PVA-*co*-PE nanofibrous membranes were deposited on a copper grid–covered roller at a 15-cm tip-to-collector distance and then dried in vacuum at 40°C for 1 hour to remove any residual solvent. ^{1}H nuclear magnetic resonance (NMR) [400 MHz, dimethyl sulfoxide (DMSO)–d_6]: δ [parts per million (ppm)] = 1.27 (d, 4H), 3.01 to 4.79 (m, 1H).

Fabrication of photoactive RNMs

In the case of BA-RNM, 0.2 g of BA and 5 g of CDI were dissolved in 20 ml of THF, and then, 0.1 g of PVA-*co*-PE nanofibrous membranes was immersed into the as-prepared solution with stirring at 60°C. After 2 hours of reaction, the resulted membranes were washed with acetone and vacuum dried. ^{1}H NMR (400 MHz, DMSO-d_6): δ (ppm) = 1.27 (d, 4H), 2.92 to 5.01 (m, 1H), 7.03 to 8.48 (m, 9H). In the case of CA-RNM, 0.2 g of CA and 5 g of CDI were dissolved in 20 ml of THF, and then, 0.1 g of PVA-*co*-PE nanofibrous membranes was immersed into the as-prepared solution with stirring at 60°C. After 2 hours of reaction, the resulted membranes were washed with acetone and vacuum dried. ^{1}H NMR (400 MHz, DMSO-d_6): δ (ppm) = 1.27 (d, 4H), 1.64 to 1.88 (m, 2H), 1.88 to 2.10 (m, 2H), 3.16 to 4.78 (m, 4H), 5.21 (d, 1H), 6.15 (d, 1H), 6.63 to 7.51 (m, 3H). In the case of BD-RNM, 0.2 g of BPTCD and 0.2 g of PPA were dissolved in 20 ml of dioxane, and then, 0.1 g of PVA-*co*-PE nanofibrous membranes was immersed into the as-prepared solution, with stirring at 80°C. After 2 hours of reaction, the resulted membranes were washed with acetone and vacuum dried. ^{1}H NMR (400 MHz, DMSO-d_6): δ (ppm) = 1.27 (d, 4H), 2.88 to 4.79 (m, 1H), 7.73 to 8.32 (m, 6H). In the case of BDCA-RNM, 0.2 g of CA and 0.2 g of PPA were dissolved in 20 ml of dioxane, and then, 0.1 g of above BD-RNM was immersed into the as-prepared solution, with stirring at 80°C. After 2 hours of reaction, the resulted membranes were washed with acetone and vacuum dried. ^{1}H NMR (400 MHz, DMSO-d_6): δ (ppm) = 1.27 (d, 4H), 1.64 to 1.84 (m, 2H), 1.86 to 2.15 (m, 2H), 2.88 to 4.82 (m, 4H), 5.21 (d, 1H), 6.15 (d, 1H), 6.59 to 8.50 (m, 9H).

Measurement of ROS

A daylight irradiation device (Spectrolinker XL-1500, Spectronics Corporation) equipped with a D65 standard light source (GE F15T8/D) was used in our experiment. The output power was set to an irradiance of 6.5 mW cm^{-2} at a distance of 16 cm from the lamp. The generation of ROS was measured in terms of the amounts of OH• and H_2O_2. The yield of OH• was quantified by the bleaching of *p*-NDA, which was a selective scavenger to quench hydroxyl radicals (*36*). In a typical experiment, 10 mg of the sample membranes was immersed into 10 ml of *p*-NDA (50 μM), which was exposed under daylight or dark conditions for a certain time. The amount of *p*-NDA left in the solution

was measured quantitatively with the absorbance at 440 nm with λ_{max}. Similarly, the amount of H_2O_2 was quantified with an indirect spectrophotometric method (*26*). In a typical test, 10 mg of the sample membranes was placed in 10 ml of deionized water, which was exposed under daylight or dark conditions for a certain time. After the exposure, 1 ml of sample solution was mixed with 1 ml of reagent I [aqueous solution of potassium iodide (66 g liter^{-1}), sodium hydroxide (2 g liter^{-1}), and ammonium molybdate tetrahydrate (0.2 g liter^{-1})] and 1 ml of reagent II [aqueous solution of potassium hydrogen phthalate (20 g liter^{-1})] with stirring for 5 min. The concentration of formed H_2O_2 in the solution was measured quantitatively with the absorbance at 351 nm with λ_{max}.

Bacterial and bacteriophage cultures

Bactericidal experiments were performed on the typical etiological bacteria, Gram-negative *E. coli* O157:H7 [American Type Culture Collection (ATCC) 700728] and Gram-positive *L. innocua* (ATCC 33090). Ten milliliters of LB broth was inoculated with a colony of *E. coli* O157 and grown at 37°C at 150 rpm. A bacterial culture with an absorbance at 600 nm of 0.4 (2×10^8 CFU ml^{-1}, as assessed by plate count) was used for further experiments. Similarly, a colony of *L. innocua* was grown in 10 ml of TSA broth at 30°C at 150 rpm until it reached an absorbance at 600 nm of 1.5 (1×10^9 CFU ml^{-1}, as assessed by plate count) and used for the following experiments. T7 bacteriophage (ATCC BAA-1025-B2) was cultured in *E. coli* BL21 cells (ATCC BAA-1025) in 10 ml of LB medium and allowed to incubate at 37°C with a shaking speed of 250 rpm. After 4 hours of incubation, 2.5 ml of chloroform was added to the solution and incubated at 37°C for 30 min with moderate shaking to lyse the remaining bacteria. Then, the solution was centrifuged for 10 min at 6000 rpm to remove any bacterial debris. The supernatant containing the phages was decanted and chilled on ice overnight at 4°C before centrifugation at 10,000 rpm for 15 min. The pellet was suspended in sterile water and diluted in PBS to obtain a titer of 1.0×10^7 PFU per milliliter (confirmed by plaque count plating).

Antibacterial assays using *E. coli* and *L. innocua*

In a typical experiment, 10 μl of the bacterial (*E. coli* or *L. innocua*) suspension was spotted on the surface of control samples (PVA-*co*-PE) or RNM samples in a size of 2×2 cm^2, and then, the samples were exposed to daylight or dark conditions for a certain time. At each time point, the samples with the bacteria were harvested by vortexing with 1 ml of deionized (DI) water, and the suspension was serially diluted ($\times 10^1$, $\times 10^2$, $\times 10^4$, and $\times 10^6$) to be plated on LB agar (*E. coli*) or TSA agar (*L. innocua*) for the bacterial enumeration. All data were standardized as 1×10^6 CFU initial load and plotted CFU. For the cyclic antimicrobial assays, after each test, the samples were sonicated for 5 min to remove the attached bacterial debris.

Fluorescence microscopy and SEM imaging of bacteria

The bacteria on the control or RNM samples were first harvested by vortexing and washed three times with PBS. For the fluorescence microscope imaging, PI and SG DNA dye were added to the bacterial suspension with a concentration of 10 μg ml^{-1}. After staining for 20 min, the bacteria were washed with PBS and rediluted in PBS. Then, the suspension was spotted on a microscope slide and examined using a laser scanning confocal microscope (Olympus FV1000). For the SEM imaging, the bacterial suspension was fixed in PBS solution containing 1 wt % of glutaraldehyde and formaldehyde for 1 hour, and then, the bacteria were rinsed with DI water three times, followed by treating with 1% of OsO_4 solution for 20 min. Bacterial samples were then dehydrated by a sequential ethanol/water mixtures with an increasing ethanol content of 25, 50, 75, 90, and 100%, respectively. Finally, the bacterial samples were placed on silver tape and coated with palladium before SEM analysis.

Antivirus assays using T7 bacteriophage

In a typical experiment, 10 μl of the phage dilution was spotted on the surface of control or RNM samples in a size of 2×2 cm^2, and then, the samples were exposed to daylight or dark conditions for a certain time. At each time point, the samples with the phages were vortexed in a tube containing 2 ml of tris-buffered saline. After serial dilution, 0.1 ml of phage solution was mixed with 0.25 ml of stationary-phase host *E. coli* BL21 (absorbance at 600 nm of approximately 1.5 outer diameter), followed by incubation for 10 min at 37°C. Afterward, 3 ml of molten LB agar at 45°C was added and mixed with the incubated bacteria plus phages, immediately poured onto a prewarmed LB agar plate, and allowed to solidify. Once the plate solidified, all the plates were inverted and incubated at room temperature overnight, and then, the plaques were counted. Phage was counted and reported as PFU ml^{-1}. All data were standardized as 1×10^5 PFU initial load and plotted PFU.

Molecular computational details

All calculations were performed using computational chemistry software package Gaussian 09 ver. 08. Initial geometries at ground state were optimized at unrestricted DFT-B3LYP/6-31+G(d,p) level of theory in conductor-like polarizable continuum model (CPCM)–H_2O solvent. Using these geometries, the nature of singlet and triplet excited energy calculations was performed using the TDDFT-B3LYP/6-31+G(d,p) level of theory in CPCM-H_2O solvent. The Gibbs free energies of all compounds were obtained by frequency calculations at unrestricted DFT-B3LYP/6-311+G(d,p) level of theory in CPCM-H_2O solvent using geometries optimized at unrestricted DFT-B3LYP/6-31+G(d,p) level of theory in CPCM-H_2O solvent. The ESP calculation was performed by single-point energy calculations with CHELPG$_5$ ESP population analysis at unrestricted DFT-B3LYP/6-31+G(d,p) level of theory in CPCM-H_2O solvent. Total electron density was first plotted and then mapped with ESP-derived charges to show a distribution of charges on the molecular structure.

Characterization

SEM images were examined by a Philips FEI XL30. UV-vis absorption spectra were collected with an Evolution 600 spectrophotometer (Thermo Fisher Scientific), and the diffuse reflection spectra were collected with a DRA-EV-600 diffuse reflectance accessory (Labsphere). ^{1}H NMR spectra were recorded on a 400-MHz Bruker Avance HD spectrometer, and DMSO-d_6 was used as a solvent. A TSI Model 8130 automated filter tester (TSI Inc.) was used to measure the filtration efficiency and pressure drop, and NaCl monodisperse aerosols with a size of 0.3 to 0.5 μm and an SD less than 1.86 were used as the model particles. The filtration QF values were defined by the formula: $QF = -\ln(1 - \eta)/\Delta p$, in which the η was the filtration efficiency and the Δp was the pressure drop.

SUPPLEMENTARY MATERIALS

Supplementary material for this article is available at http://advances.sciencemag.org/cgi/content/full/4/3/eaar5931/DC1

fig. S1. Microstructure of as-spun PVA-*co*-PE nanofibers.
fig. S2. ^{1}H NMR spectrum of PVA-*co*-PE nanofibrous membranes.
fig. S3. ^{1}H NMR spectrum of BA-RNM samples.
fig. S4. ^{1}H NMR spectrum of BD-RNM samples.

fig. S5. ^{1}H NMR spectrum of CA-RNM samples.
fig. S6. ^{1}H NMR spectrum of BDCA-RNM samples.
fig. S7. SEM images of BDCA-RNM samples with the tunable thicknesses.
fig. S8. Optical image of a BDCA-RNM sample with a large scale.
fig. S9. Detailed photoreactions of RNM samples.
fig. S10. Inter- and intramolecular hydrogen abstraction of BDCA-RNM samples.
fig. S11. Optimized molecular geometry and the predicted UV-vis absorption spectrum of DPM structure.
fig. S12. Optimized molecular geometry and the predicted UV-vis absorption spectrum of LAT structure.
fig. S13. Stability of the DPM structure by reduction in *p*-NDA.
fig. S14. Stability of the LAT structure by reduction in *p*-NDA.
table S1. Singlet excitation wavelengths and oscillator strengths of the relevant RNMs.
table S2. Gibbs free energy of the relevant reaction moieties of RNMs.

REFERENCES AND NOTES

1. C. J. E. Metcalf, J. Lessler, Opportunities and challenges in modeling emerging infectious diseases. *Science* **357**, 149–152 (2017).
2. K. J. Olival, P. R. Hosseini, C. Zambrana-Torrelio, N. Ross, T. L. Bogich, P. Daszak, Host and viral traits predict zoonotic spillover from mammals. *Nature* **546**, 646–650 (2017).
3. M. E. Halloran, I. M. Longini Jr., Emerging, evolving, and established infectious diseases and interventions. *Science* **345**, 1292–1294 (2014).
4. E. C. Holmes, G. Dudas, A. Rambaut, K. G. Andersen, The evolution of Ebola virus: Insights from the 2013–2016 epidemic. *Nature* **538**, 193–200 (2016).
5. A. Ahmad, M. U. Khan, S. Q. Jamshed, B. D. Kumar, G. S. Kumar, P. G. Reddy, S. Ajmera, Are healthcare workers ready for Ebola? An assessment of their knowledge and attitude in a referral hospital in South India. *J. Infect. Dev. Ctries.* **10**, 747–754 (2016).
6. S. Mehtar, A. N. H. Bulabula, H. Nyandemoh, S. Jambawai, Deliberate exposure of humans to chlorine-the aftermath of Ebola in West Africa. *Antimicrob. Resist. Infect. Control* **5**, 45 (2016).
7. O. Olu, B. Kargbo, S. Kamara, A. H. Wurie, J. Amone, L. Ganda, B. Ntsama, A. Poy, F. Kuti-George, E. Engedashet, N. Worku, M. Cormican, C. Okot, Z. Yoti, K.-B. Kamara, K. Chitala, A. Chimbaru, F. Kasolo, Epidemiology of Ebola virus disease transmission among health care workers in Sierra Leone, May to December 2014: A retrospective descriptive study. *BMC Infect. Dis.* **15**, 416 (2015).
8. J. Gralton, M.-L. McLaws, Protecting healthcare workers from pandemic influenza: N95 or surgical masks? *Crit. Care Med.* **38**, 657–667 (2010).
9. C. Dye, B. G. Williams, The population dynamics and control of tuberculosis. *Science* **328**, 856–861 (2010).
10. K. Bibby, L. W. Casson, E. Stachler, C. N. Haas, Ebola virus persistence in the environment: State of the knowledge and research needs. *Environ. Sci. Technol. Lett.* **2**, 2–6 (2015).
11. E. L. Beam, S. Schwedhelm, K. Boulter, C. Kratochvil, J. Lowe, A. Hewlett, S. G. Gibbs, P. W. Smith, Personal protective equipment processes and rationale for the Nebraska Biocontainment Unit during the 2014 activations for Ebola virus disease. *Am. J. Infect. Control* **44**, 340–342 (2016).
12. G. Sun, in *Antimicrobial Textiles* (Woodhead Publishing, 2016), pp. 1–3.
13. E. P. Ivanova, J. Hasan, H. K. Webb, G. Gervinskas, S. Juodkazis, V. K. Truong, A. H. F. Wu, R. N. Lamb, V. A. Baulin, G. S. Watson, J. A. Watson, D. E. Mainwaring, R. J. Crawford, Bactericidal activity of black silicon. *Nat. Commun.* **4**, 2838 (2013).
14. Y. Gao, R. Cranston, Recent advances in antimicrobial treatments of textiles. *Text. Res. J.* **78**, 60–72 (2008).
15. B. Simoncic, B. Tomsic, Structures of novel antimicrobial agents for textiles—A review. *Text. Res. J.* **80**, 1721–1737 (2010).
16. S.-H. Lim, S. M. Hudson, Application of a fiber-reactive chitosan derivative to cotton fabric as an antimicrobial textile finish. *Carbohydr. Polym.* **56**, 227–234 (2004).
17. B. Mahltig, H. Haufe, H. Böttcher, Functionalisation of textiles by inorganic sol–gel coatings. *J. Mater. Chem.* **15**, 4385–4398 (2005).
18. S. Ghayempour, M. Montazer, Micro/nanoencapsulation of essential oils and fragrances: Focus on perfumed, antimicrobial, mosquito-repellent and medical textiles. *J. Microencapsul.* **33**, 497–510 (2016).
19. B. Hilgenberg, A. Prange, L. Vossebein, in *Antimicrobial Textiles* (Woodhead Publishing, 2016), pp. 7–18.
20. A. P. Richter, J. S. Brown, B. Bharti, A. Wang, S. Gangwal, K. Houck, E. A. Cohen Hubal, V. N. Paunov, S. D. Stoyanov, O. D. Velev, An environmentally benign antimicrobial nanoparticle based on a silver-infused lignin core. *Nat. Nanotechnol.* **10**, 817–823 (2015).
21. D. V. Andreeva, D. G. Shchukin, Smart self-repairing protective coatings. *Mater. Today* **11**, 24–30 (2008).
22. J. Zhu, Q. Bahramian, P. Gibson, H. Schreuder-Gibson, G. Sun, Chemical and biological decontamination functions of nanofibrous membranes. *J. Mater. Chem.* **22**, 8532–8540 (2012).
23. Y. Si, A. Cossu, N. Nitin, Y. Ma, C. Zhao, B.-s. Chiou, T. Cao, D. Wang, G. Sun, Mechanically robust and transparent *N*-halamine grafted PVA-co-PE films with renewable antimicrobial activity. *Macromol. Biosci.* **17**, 1600304 (2017).
24. W. A. Velema, J. P. van der Berg, M. J. Hansen, W. Szymanski, A. J. M. Driessen, B. L. Feringa, Optical control of antibacterial activity. *Nat. Chem.* **5**, 924–928 (2013).
25. K. L. Yeung, W. K. Leung, N. Yao, S. Cao, Reactivity and antimicrobial properties of nanostructured titanium dioxide. *Catal. Today* **143**, 218–224 (2009).
26. J. Zhuo, in *Antimicrobial Textiles* (Woodhead Publishing, 2016), pp. 197–223.
27. A. Sirelkhatim, S. Mahmud, A. Seeni, N. H. M. Kaus, L. C. Ann, S. K. M. Bakhori, H. Hasan, D. Mohamad, Review on zinc oxide nanoparticles: Antibacterial activity and toxicity mechanism. *Nano Micro Lett.* **7**, 219–242 (2015).
28. J. Zhuo, G. Sun, Antimicrobial functions on cellulose materials introduced by anthraquinone vat dyes. *ACS Appl. Mater. Interfaces* **5**, 10830–10835 (2013).
29. Y. Li, W. Zhang, J. Niu, Y. Chen, Mechanism of photogenerated reactive oxygen species and correlation with the antibacterial properties of engineered metal-oxide nanoparticles. *ACS Nano* **6**, 5164–5173 (2012).
30. K. Nakamura, K. Ishiyama, H. Sheng, H. Ikai, T. Kanno, Y. Niwano, Bactericidal activity and mechanism of photoirradiated polyphenols against gram-positive and -negative bacteria. *J. Agric. Food Chem.* **63**, 7707–7713 (2015).
31. I. S. Farrelli, R. Toroney, J. L. Hazen, R. A. Mehl, J. W. Chin, Photo-cross-linking interacting proteins with a genetically encoded benzophenone. *Nat. Methods* **2**, 377–384 (2005).
32. S. K. Christensen, M. C. Chiappelli, R. C. Hayward, Gelation of copolymers with pendent benzophenone photo-cross-linkers. *Macromolecules* **45**, 5237–5246 (2012).
33. F. C. Fang, Antimicrobial reactive oxygen and nitrogen species: Concepts and controversies. *Nat. Rev. Microbiol.* **2**, 820–832 (2004).
34. X. Pan, G. Zhou, J. Wu, G. Bian, P. Lu, A. S. Raikhel, Z. Xi, *Wolbachia* induces reactive oxygen species (ROS)-dependent activation of the Toll pathway to control dengue virus in the mosquito *Aedes aegypti*. *Proc. Natl. Acad. Sci. U.S.A.* **109**, E23–E31 (2012).
35. H. Gruen, H. Görner, Photoreduction of 2-methyl-1-nitro-9,10-anthraquinone in the presence of 1-phenylethanol. *Photochem. Photobiol. Sci.* **7**, 1344–1352 (2008).
36. N. Liu, G. Sun, Production of reactive oxygen species by photoactive anthraquinone compounds and their applications in wastewater treatment. *Ind. Eng. Chem. Res.* **50**, 5326–5333 (2011).
37. L. Shen, H.-F. Ji, H.-Y. Zhang, Photophysical and photochemical properties of anthraquinones: A DFT study. *J. Mol. Struct.* **851**, 220–224 (2008).
38. C.-H. Lim, M. D. Ryan, B. G. McCarthy, J. C. Theriot, S. M. Sartor, N. H. Damrauer, C. B. Musgrave, G. M. Miyake, Intramolecular charge transfer and ion pairing in *N,N*-diaryl dihydrophenazine photoredox catalysts for efficient organocatalyzed atom transfer radical polymerization. *J. Am. Chem. Soc.* **139**, 348–355 (2017).
39. K. Nakamura, Y. Yamada, H. Ikai, T. Kanno, K. Sasaki, Y. Niwano, Bactericidal action of photoirradiated gallic acid via reactive oxygen species formation. *J. Agric. Food Chem.* **60**, 10048–10054 (2012).
40. J. C. Theriot, C.-H. Lim, H. Yang, M. D. Ryan, C. B. Musgrave, G. M. Miyake, Organocatalyzed atom transfer radical polymerization driven by visible light. *Science* **352**, 1082–1086 (2016).
41. A. Demeter, K. Horváth, K. Böőr, L. Molnár, T. Soós, G. Lendvay, Substituent effect on the photoreduction kinetics of benzophenone. *J. Phys. Chem. A* **117**, 10196–10210 (2013).
42. Y. Du, C. Ma, W. M. Kwok, J. Xue, D. L. Phillips, Time-resolved resonance Raman identification and structural characterization of a light absorbing transient intermediate in the photoinduced reaction of benzophenone in 2-propanol. *J. Org. Chem.* **72**, 7148–7156 (2007).
43. M. J. Smith, G. Bucher, Quenching of triplet benzophenone by benzene and diphenyl ether: A DFT study. *J. Phys. Chem. A* **114**, 10712–10716 (2010).
44. V. Barboiu, M. I. Avadanei, Chemical reactions of benzophenone photoirradiated in 1,2-polybutadiene. *J. Photochem. Photobiol. A Chem.* **222**, 170–179 (2011).
45. L. A. T. W. Asri, M. Crismaru, S. Roest, Y. Chen, O. Ivashenko, P. Rudolf, J. C. Tiller, H. C. van der Mei, T. J. A. Loontjens, H. J. Busscher, A shape-adaptive, antibacterial-coating of immobilized quaternary-ammonium compounds tethered on hyperbranched polyurea and its mechanism of action. *Adv. Funct. Mater.* **24**, 346–355 (2014).
46. W.-Y. Chen, H.-Y. Chang, J.-K. Lu, Y.-C. Huang, S. G. Harroun, Y.-T. Tseng, Y.-J. Li, C.-C. Huang, H.-T. Chang, Self-assembly of antimicrobial peptides on gold nanodots: Against multidrug-resistant bacteria and wound-healing application. *Adv. Funct. Mater.* **25**, 7189–7199 (2015).
47. Q. Wang, X. Yu, M. Libera, Reducing bacterial colonization of 3-D nanofiber cell scaffolds by hierarchical assembly of microgels and an antimicrobial peptide. *Adv. Healthc. Mater.* **2**, 687–691 (2013).
48. A. Cossu, D. Ercan, R. V. Tikekar, N. Nitin, Antimicrobial effect of photosensitized rose bengal on bacteria and viruses in model wash water. *Food Bioprocess Technol.* **9**, 441–451 (2016).
49. D. Ercan, A. Cossu, N. Nitin, R. V. Tikekar, Synergistic interaction of ultraviolet light and zinc oxide photosensitizer for enhanced microbial inactivation in simulated wash-water. *Innov. Food Sci. Emerg. Technol.* **33**, 240–250 (2016).

50. E. M. Hotze, A. R. Badireddy, S. Chellam, M. R. Wiesner, Mechanisms of bacteriophage inactivation via singlet oxygen generation in UV illuminated fullerol suspensions. *Environ. Sci. Technol.* **43**, 6639–6645 (2009).
51. X. Zhao, Y. Li, T. Hua, P. Jiang, X. Yin, J. Yu, B. Ding, Low-resistance dual-purpose air filter releasing negative ions and effectively capturing $PM_{2.5}$. *ACS Appl. Mater. Interfaces* **9**, 12054–12063 (2017).
52. S. C. Zhang, H. Liu, X. Yin, J. Y. Yu, B. Ding, Anti-deformed polyacrylonitrile/polysulfone composite membrane with binary structures for effective air filtration. *ACS Appl. Mater. Interfaces* **8**, 8086–8095 (2016).

Acknowledgments
Funding: This work is supported by the National Institute of Food and Agriculture (USDA-NIFA award #2015-68003-23411). **Author contributions:** Y.S. and G.S. designed the research. Y.S. wrote the manuscript. Z.Z. synthesized and characterized the samples. W.W., K.H., and N.N. performed the antimicrobial test. Q.F. and B.D. fabricated the electrospun nanofibrous membranes. **Competing interests:** G.S., Y.S., and Z.Z. are inventors on U.S. provisional patent application related to this work (no. 62/577,694; filed on 26 October 2017). All other authors declare that they have no competing interests. **Data and materials availability:** All data needed to evaluate the conclusions in the paper are present in the paper and/or the Supplementary Materials. Additional data related to this paper may be requested from the authors.

Submitted 27 November 2017
Accepted 7 February 2018
Published 16 March 2018
10.1126/sciadv.aar5931

Citation: Y. Si, Z. Zhang, W. Wu, Q. Fu, K. Huang, N. Nitin, B. Ding, G. Sun, Daylight-driven rechargeable antibacterial and antiviral nanofibrous membranes for bioprotective applications. *Sci. Adv.* **4**, eaar5931 (2018).